

Original Article

DOI 10.1007/s12206-021-1019-9

Keywords:

- Pleated fibrous filter
- Pressure drop
- Optimization
- Regression analysis
- Computational fluid dynamics
- Latin-hypercube sampling

Correspondence to:

Junemo Koo  
jmkoo@khu.ac.kr

Citation:

Choi, P., Ariane Santos, C., Kim, M.-K., Jung, H., Hong, D.-Y., Koo, J. (2021). Pressure drop and optimization meta-models for arbitrary low-height pleated filter shapes and flowrates. *Journal of Mechanical Science and Technology* 35 (11) (2021) 5007–5022. <http://doi.org/10.1007/s12206-021-1019-9>

Received February 1st, 2021

Revised June 30th, 2021

Accepted July 27th, 2021

† Recommended by Editor  
Yang Na

# Pressure drop and optimization meta-models for arbitrary low-height pleated filter shapes and flowrates

Paul Choi<sup>1</sup>, Christian Ariane Santos<sup>1</sup>, Min-Kun Kim<sup>2</sup>, Hyunsook Jung<sup>2</sup>, Do-Young Hong<sup>3</sup> and Junemo Koo<sup>1</sup>

<sup>1</sup>Department of Mechanical Engineering, Kyung Hee University, Yongin 17104, Korea, <sup>2</sup>Agency for Defense Development, Yuseong-Gu, Daejeon 34186, Korea, <sup>3</sup>Research Center for Nanocatalysts, Korea Research Institute of Chemical Technology (KRICT), Jang-dong, Yuseong, Daejeon 34114, Korea

**Abstract** This study delivers equations useful for low-height pleated fibrous filter design: two pressure drop equations and one set of optimum design equations applicable to arbitrary pleated filter shapes and flowrates. The pressure drop equations were derived to predict the pressure loss of the pleated filter. They were made through regression analysis with a total of 1024 CFD data. The set of optimum design equations was developed to find the optimum filter shape minimizing pressure drop. All equations were validated through the 8-fold cross-validation method and were accurate enough to replace the CFD simulations. Additionally, novel contour plots were made to describe how optimum filter geometry changes due to flowrate, height, and media permeability. The delivered equations were applied to an actual filter design problem and verified with additional CFD simulations. This study allows filter designers to predict the pressure loss and to design the optimum filter shape without any simulations.

## 1. Introduction

Since the coronavirus pandemic was declared in March 2020, purifying contaminated air has emerged as an important issue. Using pleated filters is advantageous because they have large filtration areas owing to their pleated geometry [1, 2]. Thus, pleated filters are widely used in areas requiring air purification such as medical powered air purifying respirator (PAPR) [3], chemical biological radiological and nuclear (CBRN) masks [4, 5], and so on [6]. Although collection efficiency is a significant factor for filters, reducing pressure drop is also important to curtail energy consumption for PAPRs and lower respiratory resistance for CBRN masks. The pressure drop mainly depends on not only filter material but also the filter shape parameters such as filter height, pleat pitch, media thickness, and so on [1, 2, 6-10]. In order to optimize the filter geometry to lessen pressure drop, a large number of experiments or simulations using computational fluid dynamics (CFD) are necessary. Ideally, if a generalized formula describing the correlation between pressure drop and filter shape exists, engineers can significantly reduce the time and cost for filter design optimization.

Many existing studies are investigating the relationship between pressure loss and filter geometry. However, no previous study has developed a generalized pressure drop formula for filters of arbitrary characteristics like filter shapes and permeability under arbitrary flowrate conditions. For example, some filter researchers conducted their researches without changing some of the filter characters such as filter media thickness, flowrate conditions, and so on [2, 7, 11-13]. Others carried out their studies by using only simple filter shapes, such as rectangular or triangular shapes [6, 7, 10, 12-15], thus, limiting the application of their results to various filter geometries.

Chen et al. [7] calculated the impact of filter shape on pressure drop using CFD but they considered only rectangular shaped filters and disregarded changes in filter media thickness.

Table 1. Previous studies about the relationship between pressure drop and the pleated filter shape. Further details of the filter parameters, namely, h, W, R, t, U, and VR are explained in Sec. 2.1.

Authors	Varying parameters	Fixed parameters	Inapplicable parameters	Main topic	Filter geometries	Method	$\Delta P$ equation
Chen et al. [7]	h, W, VR, U	t	R (rec)	Analysis of pressure drop using CFD results graphs	185	CFD	$\Delta^\dagger$
Tronville and Sala [11]	W, U	h, t, VR	R (tri)	Evaluation of CFD models for predicting pressure drop. Development of a regression equation of pressure drop.	1 (used for regression)	Analytical method, CFD, experiment	$\Delta$
Rebaï et al. [10]	h, W, t, U, V	-	R (rec, tri)	Development of a finite-difference model instead of commercial CFD code	9 (used for validation)	Analytical method, CFD, experiment	X
Rebai et al. [14]	h, W, t, U, V, [dust cake]	-	R (rec, tri)	Development of a finite-difference model considering dust cake effect	12 (used for validation)	Analytical method, experiment	X
Fotovati et al. [12]	W, U, VR, [pseudo-time], [particle size]	h, t	R (rec, tri)	Development of a CFD model to describe pressure drop and dust cake on the filter surface	84	Analytical method, CFD	X
Fotovati et al. [13]	h, W, U, [time], [particle size]	t, VR	R (tri)	Development of a microscale CFD model to predict pressure drop and collection efficiency over time	35	Analytical method, CFD	X
Feng et al. [6]	Not parametric study			Evaluation of CFD models for the prediction of velocity field and pressure drop	3	CFD, experiment	X
Théron et al. [2]	h, W, U	R, t, VR	-	Simultaneous study of CFD and experiments for pressure drop and velocity profile	3	CFD, experiment	X
Li et al. [9]	h, W, t, U, V, [time]	R, [particle size]	-	Analysis of effect of pleat ratio on pressure drop and cleaning capacity	6	Experiment	X
This study	h, W, R, t, U, VR	-	-	Development of the generalized pressure drop equations and the optimization equation	1024	CFD, statistical method	O

<sup>†</sup> Chen et al. [7] defined the ratio of  $\Delta P_{throat}$  to  $\Delta P_{media}$  as a function of h, W, t, and VR.

Tronville and Sala [11] developed an analytical pressure drop formula with regression analysis. However, they fixed some filter media characteristics, i.e., the media thickness, medium mass per unit area, the density of the solid material, and so on. If any of these parameters change, the equation needs to be recreated using regression once again. Rebaï et al. [10] created a semi-analytical model to replace CFD, albeit, they derived the formula using simple filter geometries such as rectangular and triangular. Furthermore, their model must be solved through a finite difference method using a system of equations, not a direct pressure drop equation.

Other than the aforementioned researches, there has been no report of a pressure loss formula study that considers all filter characteristics and flowrate conditions. Researchers have focused on other topics such as analyzing dust behavior accumulating in the filters [12, 13], finding suitable CFD models for filter analysis [6], combining the approaches of experiment and CFD [2], or investigating the deformation of the filter media due to the folding of the filter [8, 16]. These previous studies are summarized in Table 1. Filter parameters listed in the table such as h for height, W for pitch, R for folding radius, t for media thickness, U for upstream velocity, and VR for media resistance will be explained in detail in Sec. 2.1. The varying parameters column indicates parameters

that had changed more than once in the corresponding studies; thus, it is possible to identify the trends of the pressure loss due to the variations of these parameters. Inapplicable parameters are parameters that could not be covered in the corresponding studies due to simplified filter shapes such as rectangular (rec) or triangular (tri) shapes. The filter geometries column indicates the number of filter shapes used for CFD or experiment. The changes of dust particle size (in the case of Fotovati et al. [12, 13]) and VR were also included in the number.

The folding radius R has been often excluded or regarded as a constant value in the previous studies listed in Table 1. For large-height filters used in building ventilation systems, it makes sense to consider only simple shapes because the ratio of the folded portion to the total filter geometry is small. However, in the case of low-height filters used in PAPR or CBRN masks, the folding curvature should be considered as a design parameter. Indeed, Secs. 4.1 and 4.2 will describe the pressure drop variation that cannot be explained by simple filter shapes without folding curvatures.

The primary purpose of this paper is to develop a generalized pressure drop formula for arbitrary filter shapes under arbitrary flowrates according to low-height pleated filter design parameters and their ranges.

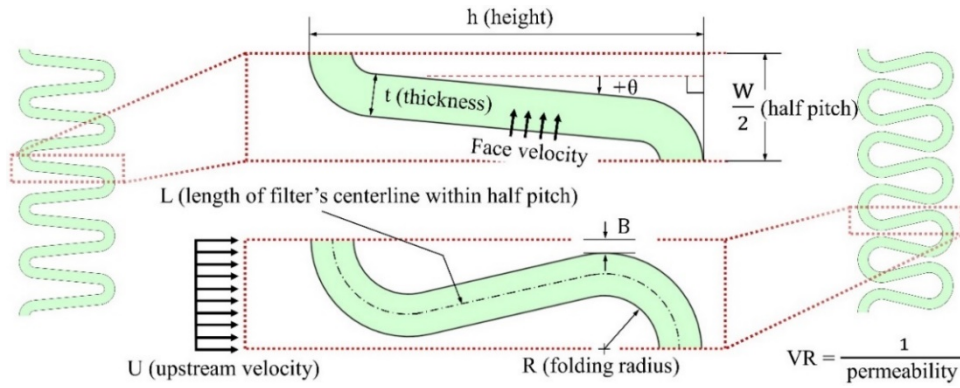


Fig. 1. The parameters of pleated filter geometry and conditions.

## 2. Theory

### 2.1 Parameters of pleated filter geometry

The parameters of the filter shape are shown in Fig. 1, where  $h$ ,  $W$ , and  $t$  are the height, pitch, and thickness, respectively. The  $R$  is the folding radius, and the  $\theta$  is defined as the pleat angle. In this paper, the clockwise rotation of  $\theta$  is considered to be a positive rotation. Two additional parameters,  $L$  and  $B$ , were defined for a better pressure drop analysis where  $L$  is the length of the filter centerline within half-pitch and the  $B$  is the breadth of the narrow passage made by a folding radius. The  $R$ ,  $L$  and  $B$  are dependent parameters, which are determined by  $h$ ,  $W$ ,  $t$ , and  $\theta$  as shown in Eqs. (1)-(3):

$$R = \frac{(2t - h)\sin\theta + \frac{W}{2}\cos\theta - t}{2(1 - \sin\theta)} \quad (1)$$

$$B = \frac{W}{2} - (R + t) \quad (2)$$

$$L = 2\left(R + \frac{t}{2}\right)\left(\frac{\pi}{2} - \theta\right) + \frac{h - 2\left\{t + R - \left(\frac{t}{2} + R\right)\sin\theta\right\}}{\cos\theta} \quad (3)$$

where the unit of  $\theta$  is [rad]. The filter geometry is determined by various combinations between four parameters among  $h$ ,  $W$ ,  $R$ ,  $t$ ,  $\theta$ ,  $L$ , and  $B$ :

$$\begin{aligned} \text{Filter shape} &= \text{function}_1(h, W, t, R) \\ &= \text{function}_2(h, W, t, \theta) \\ &= \text{function}_3(t, R, B, L) \\ &= \dots \end{aligned} \quad (4)$$

Also in Fig. 1,  $U$  denotes the upstream velocity, and  $VR$  denotes the filter resistance, which is the reciprocal of the filter media permeability. Note that  $U$  differs from face velocity which is defined as the velocity of fluid passing through the filter media. The pressure drop of the filter depends on the filter shape, upstream velocity, and the filter media:

$$\begin{aligned} \Delta P &= \text{function}(\text{Filter shape}, U, VR) \\ &= \text{function}(h, W, t, R, U, VR) \\ &= \dots \end{aligned} \quad (5)$$

Here,  $\Delta P$  represents the overall pressure drop across the filter.

### 2.2 Factors causing the pressure drop

There are two main reasons for causing the pressure drop in the pleated filters [10, 12, 13, 17]. The first reason is the filter media resistance, which is proportional to the face velocity and inversely proportional to the filter material's permeability. In this work,  $\Delta P_{\text{media}}$  is defined as the pressure drop resulting from the media resistance.

The  $\Delta P_{\text{media}}$  can be calculated using the Darcy equations [1, 6, 9, 10, 15, 18] or the Forchheimer equation [2] depending on the fiber Reynolds number defined by  $Re_{\text{fiber}} = \rho \cdot d_f \cdot V_{\text{face}} / \phi \mu$ , where  $d_f$  and  $\phi$  are the fiber diameter and the medium porosity respectively. If  $Re_{\text{fiber}} \leq 1$ , Darcy equation can be used safely [10]. The maximum face velocity in this paper is 0.085 m/s (when  $U = U_{\text{max}} = 0.25$  m/s,  $h = h_{\text{min}} = 3$  mm,  $W = W_{\text{max}} = 2$  mm,  $t = t_{\text{max}} = 0.38$  mm, and  $R = R_{\text{min}} = 0.04$  mm). Further details of the parameters' ranges are explained in Sec. 3.2). This maximum face velocity leads to the maximum  $Re_{\text{fiber}} = 0.097$  when  $d_f$  and  $\phi$  are 15  $\mu\text{m}$  and 90 % respectively. Here, the  $d_f$  is chosen as the maximum value of the fiber diameters among the 15 different filter materials [1, 9, 12, 13, 19, 20] for the rigorous calculation. For the same reason, the  $\phi$  is selected as the smallest porosity among seven different filters [12, 13]. Because the maximum  $Re_{\text{fiber}}$  is small enough, this paper used the Darcy equation and the flow in the filter media is assumed as laminar [2, 6, 10].

Through-plane permeability can be calculated by the Darcy equations [1, 6, 9, 10, 15, 18]:

$$\text{Permeability} = \frac{\mu t V_{\text{face}}}{\Delta P_{\text{media}}} \quad (6)$$

where  $\mu$  and  $V_{\text{face}}$  are the fluid dynamic viscosity and face ve-

locity, respectively. Depending on the filter material, in-plane permeability can be different from through-plane permeability [12, 13]. For simplicity, this study assumed permeability as isotropic, using Eq. (6). The second reason that causes pressure drop is the drag caused by filter geometry. The drag acting on the fluid increases as the velocity gradient increases when fluid passes through the narrow passage between the pleated surfaces. We have defined  $\Delta P_{\text{throat}}$  as the pressure drop caused by the drag, hence, the overall pressure loss  $\Delta P$  is the sum of the  $\Delta P_{\text{media}}$  and  $\Delta P_{\text{throat}}$ .

There are factors other than the two effects. For example, there are four additional factors, such as the roughness of the filter surface, the humidity [19, 20], the resistance caused by the dust on the filter [1, 9, 12, 13, 17, 20-22], and deformation of the filter media due to pleat crowding and medium compression [8, 10, 14, 16].

This study did not take into account the latter four factors because there is still no clear formula how they change with the filter shape. Furthermore, considering these factors is complicated. Therefore, it is reasonable to first formulate a pressure drop equation that only accounts for the two former factors, the media resistance and the shape of the filter, and then eventually consider the effects of the aforementioned four factors in future research.

### 3. Research method

#### 3.1 Overall methodology

As shown in Eq. (4), filter geometry is determined by a combination of four filter parameters chosen from  $h$ ,  $W$ ,  $R$ ,  $t$ ,  $\theta$ ,  $L$ , and  $B$ . Among the list,  $h$ ,  $W$ ,  $R$ , and  $t$  were selected to make the generalized pressure drop formula, Eq. (5). Thus,  $\Delta P = \text{function}(h, W, t, R, U, VR)$  is generated by regression analysis for the considered parameters. A large number of data are needed to develop the function. That is,  $\Delta P$  information is required for all possible combinations between  $h$ ,  $W$ ,  $t$ ,  $R$ ,  $U$ , and  $VR$ . This study uses the Latin-hypercube sampling (LHS) method proposed by McKay et al. [23] to generate the combinations. LHS method is a widely used technique for which accurate results can be obtained by sampling a distribution that is more evenly distributed than other methods such as random sampling or stratified sampling [23]. This approach divides each parameter into equal intervals and then combines each parameter statistically. The pressure drop equation can be accurately obtained through the LHS method despite a relatively small extracted data.

The specific methods of this study are as follows: The first step is to extract the 1024 filter models by using the LHS method. The next step is the CFD calculation of the models. The third step is to formulate the pressure drop equations through regression analysis. The fourth step is to make an optimization algorithm to find the optimum filter shape to minimize pressure loss using one of the pressure drop equations. The final step is to formulate the optimization equation that can

derive optimum filter shapes immediately.

#### 3.2 Ranges of the parameters

This study determined the ranges of the parameters based on the design of the filter in the CBRN gas mask canister. There are two reasons why the CBRN canister was selected.

First, the assumption of neglecting the dust effect is quite reasonable. CBRN canister consists of two porous structures, a filter layer and an activated carbon layer [4]. The service life of the canister is just a few hours in the contaminated area since CBRN weapons breakthrough the activated carbon layer. As a result, there is not enough time for the dust to stick to the filter surface. The specific time scale of the dust caking and breakthrough of the CRBN canister is explained in Appendix A.1.

Secondly, the filter shape of the canister must be optimized for reducing not only respiration resistance but also the filter height, that is, the smaller filter height  $h$ , the better freedom of movement the user has.

In this study, the pitch  $W$  and the height  $h$  are in the range of 1.08-2 mm and 3-6 mm, respectively. The range of the VR value is between  $1.0 \times 10^{11}$  to  $1.4 \times 10^{12} \text{ m}^{-2}$  and the thickness  $t$  is from 0.3 to 0.38 mm, as referred to the low-permeability filter materials in other studies [6, 11, 24]. The range of upstream velocity  $U$  was chosen from 0.01 m/s to 0.25 m/s, considering the mean inspiratory flow at moderate workloads [25] and the diameter of the gas mask canister [4]. The ranges of  $R$  and  $\theta$  depend on other parameters, as shown in Fig. 1. The actual maximum and minimum values of the  $\theta$  occur when  $R = 0$  mm, and when  $B = 0$  mm, respectively. However, for the convergence of CFD calculation,  $\theta_{\text{max}}$  was set at  $R = 0.04$  mm, and  $\theta_{\text{min}}$  was chosen at  $B = 0.07$  mm. The ranges of the parameters needed to develop the pressure drop equations were summarized in Table 2.

#### 3.3 Latin-hypercube sampling

This paper extracted the 1024 filter models through LHS method for the considered range shown in Table 2. The specific method and the data point plots are shown in Appendix A.2. The filter geometries are formed by specifying the parameters  $h$ ,  $W$ ,  $t$ , and  $R$ . The  $U$  and  $VR$  are used as CFD calculation conditions.

#### 3.4 Numerical method

##### 3.4.1 Simulation domain and boundary condition

The calculation domain is shown in Fig. 2(a). The calculation area is two-dimensional and only the half-pitch is considered using symmetry conditions to reduce unnecessary calculations. Near the inlet and outlet, the mesh is the structured rectangular mesh while the rest of the domain has the unstructured triangular mesh. The inlet velocity and pressure-outlet conditions are specified as  $U$  and atmospheric pressure, respectively. The

Table 2. Ranges of parameters for Latin-hypercube sampling to develop the pressure drop equations.

Parameters		Min	Max	Unit
h	Height	3	6	[mm]
W	Pitch	1.08	2	[mm]
t	Thickness	0.30	0.38	[mm]
U	Upstream velocity	0.01	0.25	[m/s]
VR	Inverse of permeability	$1.0 \times 10^{11}$	$1.4 \times 10^{12}$	[m <sup>-2</sup> ]
$\theta$	Pleat angle	$\theta_{\max}^{\dagger}$	$\theta_{\min}^{\ddagger}$	[rad]

<sup>†</sup>  $\theta = \theta_{\min}$  when  $B = 0.07$  mm (when  $R = R_{\max} = W/2 - 0.07 - t$ )

<sup>‡</sup>  $\theta = \theta_{\max}$  when  $R = R_{\min} = 0.04$  mm

permeability of the filter is calculated as the reciprocal of VR. The working fluid is air with a dynamic viscosity of  $\mu = 1.7894 \times 10^{-5} \text{ kg} \cdot \text{m}^{-1} \cdot \text{s}^{-1}$ , and density of  $\rho = 1.225 \text{ kg} \cdot \text{m}^{-3}$ .

The flow in the filter media is assumed as laminar [2, 6, 10]. The porous media model is used to calculate the pressure drop in the filter media according to Darcy's equation, Eq. (6). Note that in Sec. 2.2, this paper decided to use the Darcy equation instead of the Forchheimer equation.

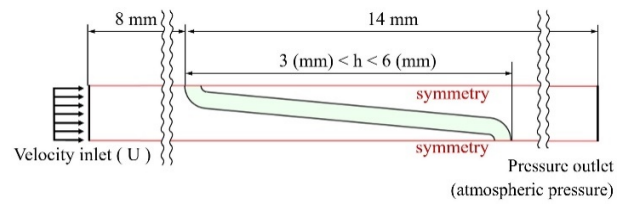
The locations where the large gradients of pressure and velocity occur are different depending on the filter geometries. Therefore, the location of the fine mesh should vary with filter shape. To create mesh economically, this paper classified filter geometries into three groups: (1) thin group, (2) small radius group, and (3) large radius group, as shown in Fig. 2(b). The fine meshes were generated on the ash-colored locations for each group.

### 3.4.2 Calculation

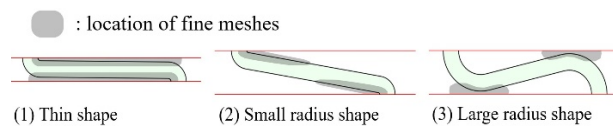
The steady-state Navier-Stokes equation was used as the governing equation for CFD calculation. The equation was solved by Fluent 19.5 (Ansys, Canonsburg, PA, USA) commercial code based on the finite volume method. To enhance the accuracy of the calculation, this study used green-Gauss node-based, PRESTO, and warped-face gradient correction schemes. For all 1024 models, the calculation residual is less than  $2 \times 10^{-5}$ . The residual convergence criteria include continuity, velocity, turbulent kinetic energy, dissipation rate of turbulent kinetic energy, stress, and the pressure drop. The pressure drop was estimated as the static pressure difference between the inlet and the outlet.

### 3.4.3 Turbulent model

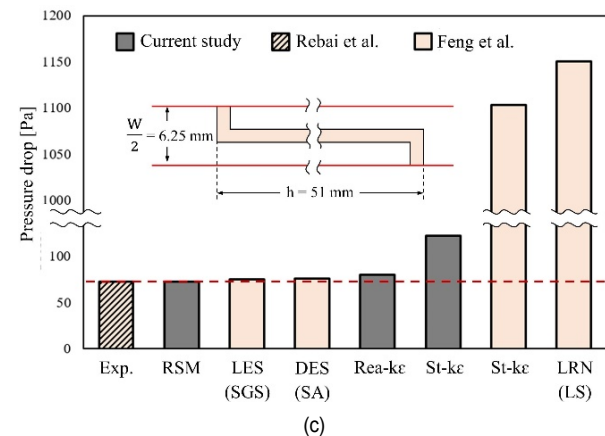
The flow regime in the computational domain except for the filter interior can be turbulent [6], thus a proper turbulent model must be used, not a simple laminar model. If  $\Delta P_{\text{media}}$  is dominant and  $\Delta P_{\text{throat}}$  is negligible in  $\Delta P$  (for high VR and large W), almost any turbulent models can accurately predict the pressure loss. Indeed, Feng et al. [6] showed that all five different turbulent models correctly predicted pressure loss of sparsely-pleated filters ( $h = 50$  mm,  $W = 50$  mm,  $VR = 1.20 \times 10^{11} \text{ m}^{-2}$ ). However, when  $\Delta P_{\text{throat}}$  is important (for low VR or small W),



(a)



(b)



(c)

Fig. 2. CFD method: (a) the calculation domain; (b) the locations of fine meshes in the three types of filter geometry: Thin shape, small radius shape, and large radius shape; (c) accuracy of CFD models compared to experimental [10] and numerical [6] data.

some CFD models cannot predict pressure drop exactly. For example, Tronville and Sala [11] showed that the standard  $k-\epsilon$  model failed to predict pressure loss and that renormalization-group (RNG)  $k-\epsilon$  model was less accurate than the Reynolds stress model on a densely-pleated filter ( $h = 25$  mm,  $W = 3.2$  mm,  $VR = 1.33 \times 10^{11} \text{ m}^{-2}$ ).

Therefore, a suitable CFD model should be selected for the accurate calculation and the accuracy of CFD models should be verified using experimental data for large enough  $\Delta P_{\text{throat}}$ . Feng et al. [6] analyzed the accuracy of turbulent models in comparison with the suitable data from Rebaï et al. [10]. They checked that the ratio of  $\Delta P_{\text{throat}}$  to  $\Delta P$  was 66 % under the data conditions ( $U = 2.4$  m/s,  $h = 51$  mm,  $W = 12.5$  mm,  $t = 1.45$  mm,  $VR = 2.8 \times 10^9 \text{ m}^{-2}$ , rectangular-shaped filter), thus the experimental data is suitable for the validation. Accordingly, this study tested additional turbulent models. Due to the high upstream velocity, the calculations were hard to be converged. Thus, dense inflation layers of mesh near the media surface were generated, resulting to 2603271 total mesh count for the geometry.

The results are shown in Fig. 2(c). In the figure, the names of CFD models are abbreviated: RSM for Reynolds stress model, LES (SGS) for large eddy simulation model (Smagorinsky-Lilly

model), DES (SA) for detached eddy simulation model (Spalart-Allmaras), Rea- $k\epsilon$  for Realizable  $k\epsilon$  model, St- $k\epsilon$  for standard  $k\epsilon$  model, and LRN (LS) for low Reynolds number  $k\epsilon$  model.

Fig. 2(c) shows that RSM, LES and DES models have high accuracy. The result can be explained by the filter geometry and eddy direction. For filter CFD, anisotropic eddy must be analyzed because the eddy intensity depends on the XYZ direction due to the pleated filter geometry. These three models consider anisotropic eddies. The RSM calculates the eddy-viscosity differently depending on the XYZ directions. The LES model calculates large eddies directly without using simple isotropic modeling. The DES model uses similar method as the LES model in the turbulent domain. On the other hand, the  $k\epsilon$  and LRN models are solved with an isotropic eddy-viscosity hypothesis, thus, have poor accuracy for filter CFD. This study therefore selected RSM as the turbulent model because of its high accuracy.

Note that for the St- $k\epsilon$  model, the result of the current study is quite different from that of Feng et al. [6]. It can therefore be concluded that even with the same turbulence model, the simulation accuracy will depend on other factors such as mesh design, the specific calculation methods described in Sec. 3.4.2, and so on.

### 3.5 Grid independence

It is impossible to conduct all grid independence tests for 1024 models. Note that in Sec. 3.4.1, the filter models are classified into three groups and each group has different mesh distribution. This paper made one or two test conditions that made it most challenging to converge the CFD calculations for each group. For example, U, VR, and t in the test conditions were designated as the maximum values which are  $U_{\max}$ ,  $VR_{\max}$ , and  $t_{\max}$  of Table 2, respectively, to make the maximum gradients of pressure and velocity. For the test condition of the large radius group, the folding radius R was assigned as  $R_{\max}$  to make high-velocity gradient by making B minimal. If a CFD calculation in the mesh model is converged under the extreme conditions (test conditions), then the calculation in the mesh model will be easily converged under the not extreme conditions (1024 models' conditions).

This study checked the variation of pressure drop by increasing the mesh number for each test condition. If the pressure drop changed below 0.4 % even if the number of grids increased by more than 20 %, the corresponding mesh model was chosen. The average mesh number of thin shape group, small radius group, and large radius groups are 282000, 170000, and 228000, respectively. The mean mesh size of the 1024 models is 218000.

### 3.6 Development of the pressure drop equation

After 1024 CFD calculations, the regression analysis was

Table 3. Accuracy of the pressure drop equations, Eqs. (7) and (8).

	Eq. (7)	Eq. (8)
Training set accuracy		
MAE [Pa]	1.409	2.440
RMSE [Pa]	2.418	3.802
MAPE [%]	1.534	2.965
$r^2$ [-]	0.9993	0.9982
Test set accuracy (8-fold cross-validation)		
MAE [Pa]	1.495	2.502
RMSE [Pa]	2.701	3.918
MAPE [%]	1.627	3.044
$r^2$ [-]	0.9991	0.9981

used to derive the pressure drop equations with a total of 1024 CFD data. This paper used stepwise regression method minimizing Akaike information criterion (AIC) to avoid the overfitting problem. The smaller the AIC, the better the prediction accuracy of the regression equation. This paper developed two alternative pressure drop equations using different numbers of the parameters because both equations have pros and cons:

$$\begin{aligned} \Delta P &= \text{function}(h, W, t, R, \theta, B, L, U, VR) \\ &= \exp\left(C_0 + \sum_{i=1}^9 C_i \cdot X_i + \sum_{j=1}^n \sum_{i=1}^m C_{ij} \cdot X_i \cdot X_j\right) \end{aligned} \quad (7)$$

$$\begin{aligned} \Delta P &= \text{function}(h, W, t, R, U, VR) \\ &= \exp\left(C_0 + \sum_{i=1}^6 C_i \cdot X_i + \sum_{j=1}^n \sum_{i=1}^m C_{ij} \cdot X_i \cdot X_j\right) \end{aligned} \quad (8)$$

Note that each right-hand side of the equations is taken natural exponential function (exp). The mean factor levels  $X_k$  and coefficient  $C_k$  are shown in Table A.1. The parameters, except for  $\theta$ , were taken natural logarithm (ln) and were used as  $X_k$  to enhance accuracy. The units of h, W, t, R, L, and B are [mm]. The units of  $\theta$ , U, VR, and  $\Delta P$  are [rad], [m/s], [ $m^2$ ] and [Pa] respectively. The factors in the table are arranged in order of importance. ANOVA test was performed to sort the factors of the equations from the largest F-value. However, because there are interaction effects, the importance of the variables VR, U, h, W, t, and R were dispersed. The order of importance for each parameter was described in detail in Sec. 4.1.

The regression equations should be validated not only on training data but also on test data. Training data are the data used in the regression process, while test data are the ones not used in the development of the regression model since they are assigned for the purpose of evaluating the prediction accuracy of the regression model. This study chose 8-fold cross-validation method to check the prediction accuracy. Table 3 shows the accuracy of the equations where the abbreviated criteria are: mean absolute error (MAE), root mean square error (RMSE), mean absolute percentage error (MAPE) and coefficient of determination ( $r^2$ ).

Considering the average pressure drop of 1024 filter models

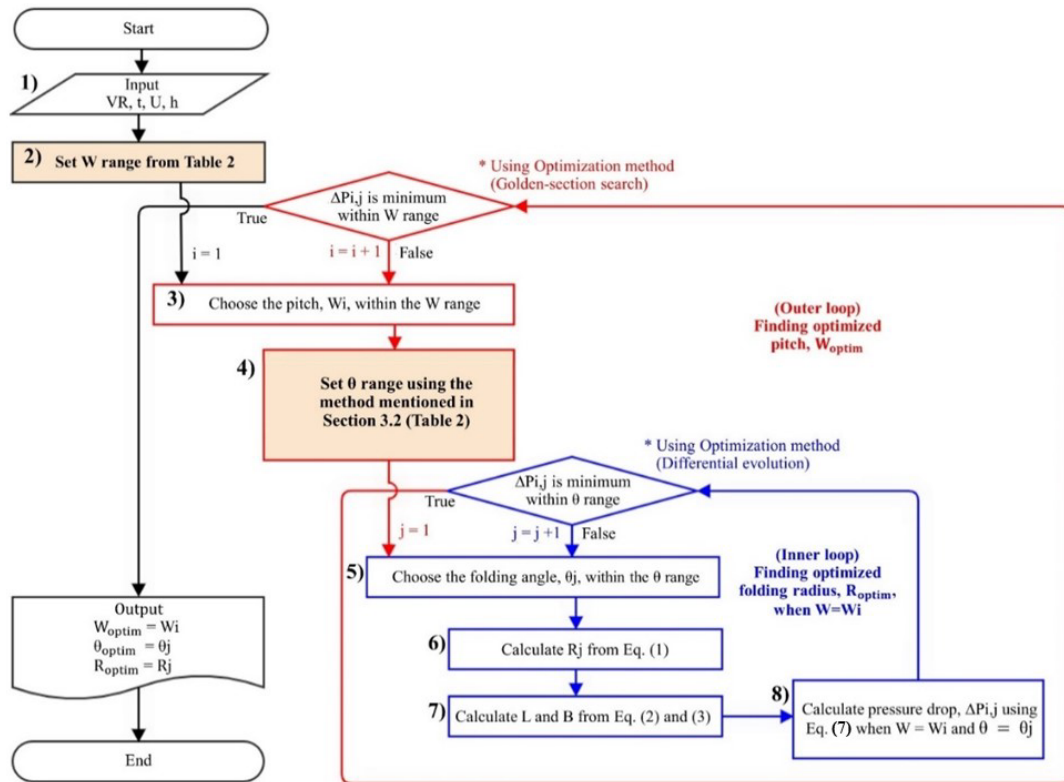


Fig. 3. Flowchart for filter shape optimization.

is 107.18 Pa, the MAE and RMSE of the two equations are good enough to replace CFD calculations. Therefore, the derived equations can instantaneously calculate pressure loss with an arbitrary condition without additional CFD simulations. Note that the two equations are applicable only within the parameters' ranges shown in Table 2.

Eqs. (7) and (8) have both an advantage and a disadvantage. In terms of MAE, RMSE, MAPE and  $r^2$  shown in Table 3, Eq. (7) yielded better results than Eq. (8). These data show that  $\theta$ , B and L enhanced the prediction accuracy of the pressure drop equation, and therefore indicate that Eq. (7) has better precision than Eq. (8). However, the three additional parameters of Eq. (7) must be calculated using Eqs. (1)-(3) and  $\theta$  must be obtained by using iterative numerical methods because Eq. (1) has a complex form. On the other hand, Eq. (8) is simpler and straightforward but is relatively inaccurate when compared with Eq. (7). Therefore, the selection of which equation is best depends on whether high accuracy is required or if speed precedes veracity. Eq. (7) is ideal for the former while Eq. (8) could be used for quick calculation scenarios.

### 3.7 Optimization of the filter shape

One of the important reasons for creating a pressure drop equation is to find out the optimal filter geometry that minimizes pressure loss. VR and t are determined by filter material while U depends on the conditions of filter use. If the filter height h is

fixed for spatial reasons, it is only necessary to find optimum W and R to minimize pressure loss.

#### 3.7.1 Optimization algorithm

In this study, the optimal filter geometry was determined by applying an optimization algorithm to Eq. (7) due to its high prediction accuracy. The flowchart of the algorithm to obtain the optimal pitch,  $W_{\text{optim}}$ , and the optimal folding radius,  $R_{\text{optim}}$ , is shown in Fig. 3. The two loops are used because the range of R varies with W as mentioned in Sec. 3.2. The outer loop and inner loops indicate the steps to find the  $W_{\text{optim}}$  and the  $R_{\text{optim}}$ , respectively. The methods are as follows: Once the user enters the information about filter media and conditions (Step 1), the range of W is calculated using Table 2 (Step 2). If W changes in the outer loop (Step 3), the corresponding range of  $\theta$  is determined using the method mentioned in Sec. 3.2 (Step 4). Within the  $\theta$  range, the inner loop finds the  $\theta$  and R of which the pressure loss is minimal (Steps 5-8). The outer loop finds  $W_{\text{optim}}$  within the W range, using the pressure drop information from the inner loop. The gold section search [26] and differential evolution methods [27] are used as optimization techniques in the outer loop and inner loop respectively.

#### 3.7.2 Development of the optimization equation

For the ease of finding optimum filter design using the optimization process in Fig. 3, this study suggests a set of optimization equations that calculates  $W_{\text{optim}}$  and  $R_{\text{optim}}$  immediately

Table 4. Accuracy of the optimization equation, Eq. (9).

	$W_{\text{optim}}$ equation	$R_{\text{optim}}$ equation
Training set accuracy		
MAE [Pa]	$5.44 \times 10^{-4}$	$8.09 \times 10^{-5}$
RMSE [Pa]	$8.08 \times 10^{-4}$	$1.14 \times 10^{-4}$
MAPE [%]	$4.56 \times 10^{-2}$	$1.10 \times 10^{-1}$
$r^2$ [-]	0.999913	0.999921
Test set accuracy (8-fold cross-validation)		
MAE [Pa]	$5.92 \times 10^{-4}$	$9.25 \times 10^{-5}$
RMSE [Pa]	$8.69 \times 10^{-4}$	$1.29 \times 10^{-4}$
MAPE [%]	$4.96 \times 10^{-2}$	$1.27 \times 10^{-1}$
$r^2$ [-]	0.999899	0.999898

when  $h$ ,  $VR$ ,  $U$ , and  $t$  are determined:

$$\begin{cases} W_{\text{optim}} = \text{function}(h, t, U, VR) \\ = C_0 + \sum_{i=1}^n C_i \cdot X_i + \sum_{j=1}^l \sum_{i=1}^m C_{ij} \cdot X_i \cdot X_j \\ R_{\text{optim}} = \text{function}(h, t, U, VR) \\ = C_0 + \sum_{i=1}^n C_i \cdot X_i + \sum_{j=1}^l \sum_{i=1}^m C_{ij} \cdot X_i \cdot X_j \end{cases} \quad (9)$$

where  $C_k$  is coefficient and  $X_k$  is the factor levels for  $h$ ,  $t$ ,  $\ln(VR)$ ,  $\ln(U)$ ,  $h^2$ ,  $t^2$ ,  $(\ln(VR))^2$ , and  $(\ln(U))^2$ . The units of  $W_{\text{optim}}$ ,  $R_{\text{optim}}$ ,  $h$ , and  $t$  are [mm]. The units of  $U$  and  $VR$  are [m/s] and [m<sup>-2</sup>], respectively. Note that there is no exponential function on the right-hand side of the equation, unlike Eqs. (7) and (8). This study first extracted 12288 combinations of  $h$ ,  $t$ ,  $U$ , and  $VR$  statistically. This paper then found in total, 12288 sets of  $W_{\text{optim}}$  and  $R_{\text{optim}}$  using the algorithm shown in Fig. 3. Only 7558 out of the 12288 data were used for the regression analysis because the remaining 4730 data were inaccurate since their  $W_{\text{optim}}$ s were smaller than the extreme value (1.08 mm) shown in Table 2. This study used the stepwise regression method minimizing AIC and the result is shown in Table A.2. Like Table A.1, the factors in the Table A.2 are arranged in order of importance through ANOVA test.

The accuracy of Eq. (9) was evaluated using the 7558 data. Table 4 shows the mean absolute percentage error (MAPE) for  $W_{\text{optim}}$  equation on test data is only at 0.0496 % and the  $R_{\text{optim}}$  equation score is at 0.127 %. Thus, the prediction accuracy of Eq. (9) is very high, which means that the set of equations is accurate enough to replace the optimization algorithm of Fig. 3. Note that the equation set is accurate only within the ranges of parameters in Table 2. For example, if the output of  $W_{\text{optim}}$  equation is smaller than 1.08 mm or greater than 2 mm, the results are unreliable.

## 4. Results and discussion

### 4.1 Impact of parameters on pressure drop

This paper evaluated the importance of  $h$ ,  $W$ ,  $R$ ,  $t$ ,  $U$ , and  $VR$

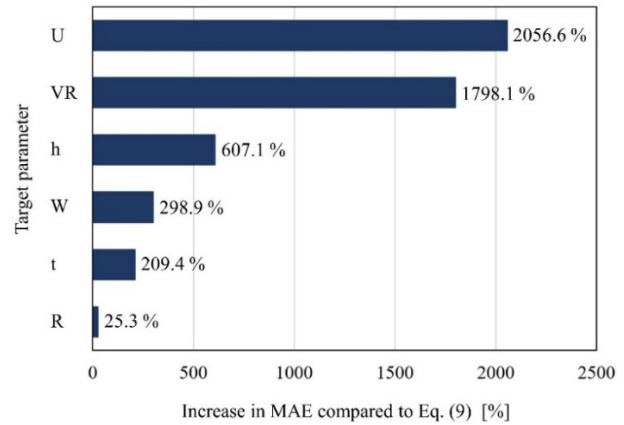


Fig. 4. Order of importance of each parameter relevant to the pressure drop estimation.


for pressure drop using Eq. (8). T-test and analysis of variance (ANOVA) are widely used statistical methods for assessing the importance of parameters in a regression model. However, the methods are not appropriate for models that have interaction effects like Eq. (8) because the importance of the parameters can be dispersed. For example, it is hard to evaluate the importance of  $U$  in Eq. (8) because the effect of  $U$  is separated by three factors which are  $\ln(U)$ ,  $\ln(VR) \cdot \ln(U)$ , and  $\ln(U) \cdot \ln(W)$  as shown in Table A.1. Therefore, this study used a new unconventional method. This method was based on a simple assumption: if a regression model is developed without an important parameter, the accuracy of the model will be significantly reduced.

The specific procedures are as follows: First, a target parameter to be checked for importance was selected from  $h$ ,  $W$ ,  $t$ ,  $R$ ,  $VR$ , and  $U$ . Second, a new pressure drop equation was developed using the remaining five parameters, except the target, using the method applied in developing Eq. (8) discussed in Sec. 3.6. For instance, if  $VR$  is the target, a new pressure drop equation is made with the combinations between  $\ln(h)$ ,  $\ln(W)$ ,  $\ln(t)$ ,  $\ln(R)$ , and  $\ln(U)$ . Third, the increase in mean absolute error (MAE) of the new equation in comparison with Eq. (8) is calculated:

$$\begin{aligned} \text{Increase in MAE} \\ = \left( \frac{MAE|_{\text{New}} - MAE|_{\text{Eq. (8)}}}{MAE|_{\text{Eq. (8)}}} \right) \times 100 [\%] \end{aligned} \quad (10)$$

where  $MAE|_{\text{NEW}}$  is the MAE of the new equation made without the target parameter while  $MAE|_{\text{Eq. (8)}}$  is the MAE of Eq. (8). A significant increase in MAE means that the absence of the target parameter is fatal to the accuracy of the equation, therefore, the parameter is important. These procedures were repeated six times by changing the target. The result is shown in Fig. 4 where the order of importance in descending order is  $U > VR \gg h > W > t > R$ . Therefore when filter media ( $VR$  and  $t$ )



 : The domain out of the model's calculation range where  $W_{\text{optim}} < 1.08$  mm.

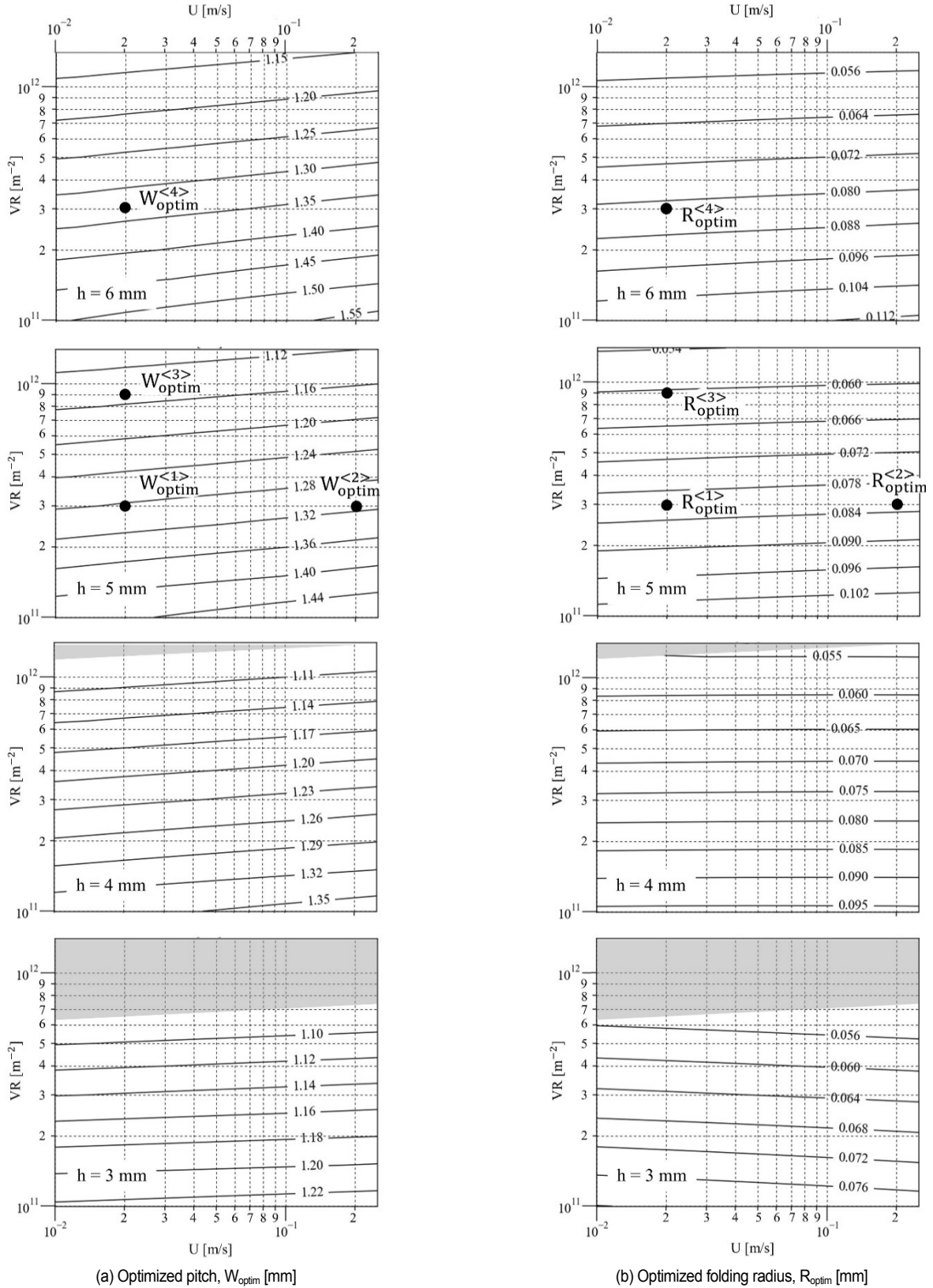


Fig. 5. Contour plots (a) of the optimum pitch  $W_{\text{optim}}$ ; (b) of the optimum folding radius  $R_{\text{optim}}$  as a function of U and VR when  $t$  is 0.38 mm.

and operation condition ( $U$ ) are given, the filter engineer should design in the order of  $h$ ,  $W$ , and  $R$ . Although the effect of  $R$  is relatively small, the  $R$  should be used as a design parameter because it can improve the accuracy by 25.3 %. Note that the importance of parameters depends on their ranges in Table 2. For example, if the range of  $t$  is 0.3-3.8 mm rather than 0.3-0.38 mm, the importance of  $t$  will increase.

#### 4.2 Contour plot of the optimum points

Figs. 5(a) and (b) show the optimum filter shapes,  $W_{\text{optim}}$  and  $R_{\text{optim}}$ , as a function of  $U$  and  $VR$  when  $t = 0.38$  mm. The horizontal and vertical dashed lines are about  $VR$  and  $U$  respectively while the solid lines represent levels of  $W_{\text{optim}}$  and  $R_{\text{optim}}$ . Thus, the filter shape should be designed with the contour values to minimize the pressure drop. For example, when  $t$ ,  $h$ ,  $VR$ , and  $U$  are 0.38 mm, 5 mm,  $3 \times 10^{11} \text{ m}^{-2}$  and 0.02 m/s, respectively, the corresponding  $W_{\text{optim}}$  is 1.28 mm and  $R_{\text{optim}}$  is 0.081 mm ( $W_{\text{optim}}^{(1)}$  and  $R_{\text{optim}}^{(1)}$ ). Each of the eight (8) contour graphs was made with 675 optimum points, calculated through the algorithm shown in Fig. 3. The ash-colored zone indicates inaccurate contour domain because  $W_{\text{optim}} < 1.08$  mm and is out of the valid calculation range shown in Table 2.

As mentioned in Sec. 2.2, the optimum filter shape is determined by the trade-off between the  $\Delta P_{\text{media}}$  and  $\Delta P_{\text{throat}}$  [7, 10]. When  $W$  decreases,  $V_{\text{face}}$  decreases because the total area of the filter increases, thus  $\Delta P_{\text{media}}$  decreases from Eq. (6). On the other hand, if  $W$  increases, the pleat spacing increases, thus  $\Delta P_{\text{throat}}$  decreases. Therefore, if we need to minimize  $\Delta P_{\text{media}}$ , then  $W$  should be small. On the other hand, to minimize  $\Delta P_{\text{throat}}$ ,  $W$  should be large.

Fig. 5(a) shows useful information for optimizing the pitch. First, as  $U$  increases,  $W_{\text{optim}}$  also increases (from  $W_{\text{optim}}^{(1)}$  to  $W_{\text{optim}}^{(2)}$ ) to reduce  $\Delta P_{\text{throat}}$ . This result is consistent with those of other researchers [10, 11]. This shows that  $\Delta P_{\text{throat}}$  increases faster than  $\Delta P_{\text{media}}$  when  $U$  increases. Second, as  $VR$  increases,  $W_{\text{optim}}$  decreases (from  $W_{\text{optim}}^{(1)}$  to  $W_{\text{optim}}^{(3)}$ ) to reduce  $\Delta P_{\text{media}}$  as expected from Darcy's estimation, Eq. (6). Third, when the remaining conditions are fixed,  $W_{\text{optim}}$  increases as  $h$  increases (from  $W_{\text{optim}}^{(1)}$  to  $W_{\text{optim}}^{(4)}$ ). This is the same result as Chen et al. [7]. The reason for the increase in  $W_{\text{optim}}$  is to reduce the  $\Delta P_{\text{throat}}$ , which has increased sharply due to the increase in  $h$ .

With the above information, filter designers will be able to design the filter geometry with ease. For example, suppose you are designing filters in gas masks. For children with lower breathing volume, the pitch,  $W$ , will need to be designed smaller than adult products considering the lower air flowrate, hence lower  $U$ . In the case of gas masks made with high  $VR$  filter for high dust collection efficiency, the  $W$  will need to be designed small. However, for electrostatic cotton filters,  $W$  can be designed large since its  $VR$  is low.

It is difficult to intuitively understand the principle of  $R_{\text{optim}}$  change through Fig. 5(b). Therefore, further CFD simulations were conducted to investigate the effect of  $R$ . Figs. 6(a)-(c) show the folding radius effect by changing  $R$  from 0.05 to

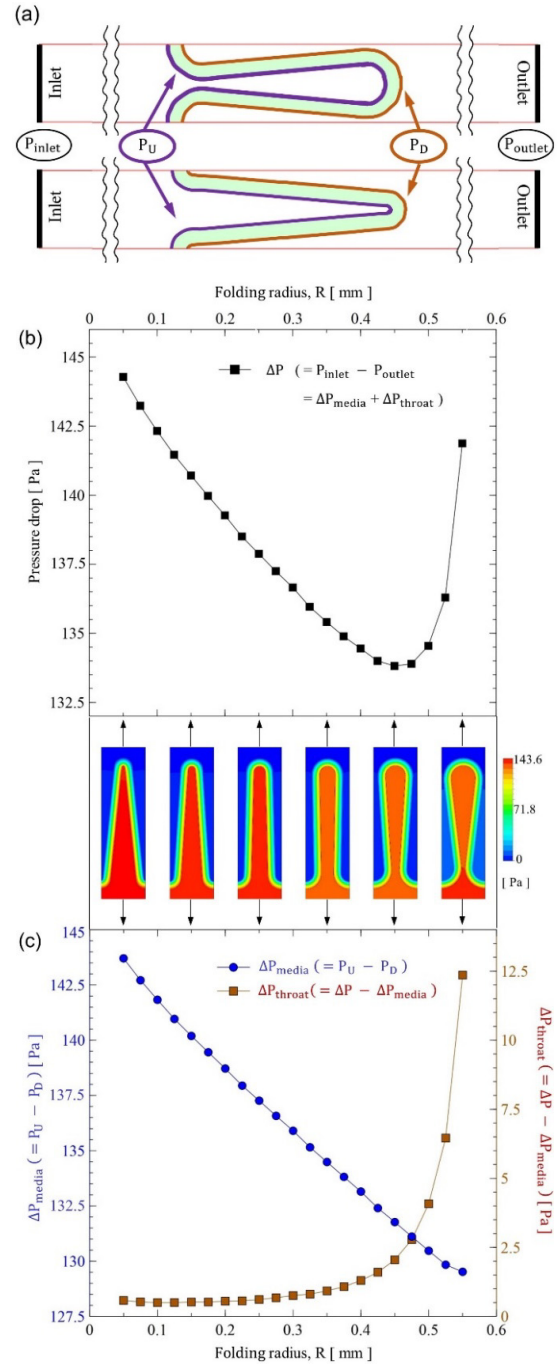


Fig. 6. The analysis of the effect of folding radius through additional CFD calculations: (a) pressure measurement areas for the calculation of pressure drops; (b) the overall pressure drop  $\Delta P$ ; (c) the trade-off between  $\Delta P_{\text{media}}$  and  $\Delta P_{\text{throat}}$  as a function of folding radius (note that 0.45 mm is not  $R_{\text{optim}}$  because it is calculated with fixed  $W$ .  $R_{\text{optim}}$  should be calculated through the algorithm in Fig. 3 which finds both  $W_{\text{optim}}$  and  $R_{\text{optim}}$  simultaneously).

0.55 mm when the remaining parameters  $W$ ,  $h$ ,  $VR$ ,  $U$ , and  $t$  were fixed at 2 mm, 6 mm,  $10^{12} \text{ m}^{-2}$ , 0.122 m/s, and 0.38 mm respectively. The three kinds of pressure drop were calculated through area-weighted average method with the four (4) pres-

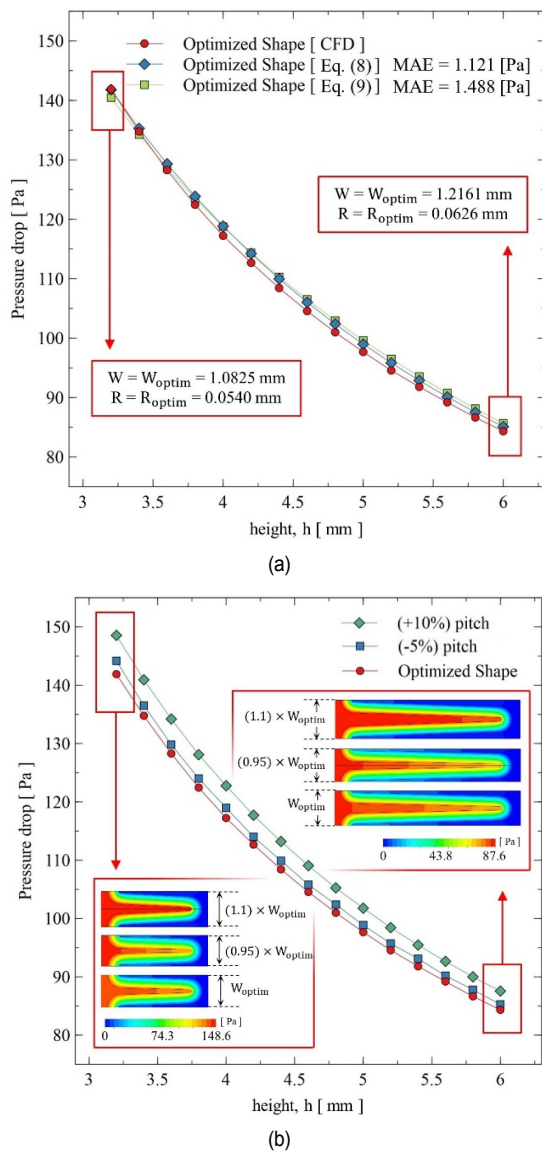


Fig. 7. The application of Eqs. (7) and (8) to a commercial filter when  $h = 3.2 - 6$  mm with  $U$  fixed at  $0.13$  m/s: (a) the validation of Eqs. (7) and (8) by comparing pressure drop of optimum filter shapes results with the CFD result; (b) the validation of Eq. (9) through comparison with the CFD results for different pitch sizes.

sure measurement areas (inlet, outlet, and two filter media surfaces) shown in Fig. 6(a), i.e.,  $\Delta P = P_{\text{inlet}} - P_{\text{outlet}}$  and  $\Delta P_{\text{media}} = P_U - P_D$  and  $\Delta P_{\text{throat}} = \Delta P - \Delta P_{\text{media}}$ . Fig. 6(b) shows the overall pressure drop  $\Delta P$ . The minimum pressure drop occurs when  $R$  is  $0.45$  mm. Note that  $0.45$  mm is not  $R_{\text{optim}}$  because it is calculated with fixed  $W$ .  $R_{\text{optim}}$  should be calculated through the algorithm in Fig. 3 which finds both  $W_{\text{optim}}$  and  $R_{\text{optim}}$  simultaneously. Fig. 6(c) shows the trade-off between  $\Delta P_{\text{media}}$  and  $\Delta P_{\text{throat}}$  relative to  $R$ . Pressure drop at media ( $\Delta P_{\text{media}}$ ) has a downward trend due to the increase in filtration area while pressure drop at throat ( $\Delta P_{\text{throat}}$ ) increases due to smaller pleat spacing. This shows that  $R_{\text{optim}}$ , like  $W_{\text{optim}}$ , is determined by the trade-off between  $\Delta P_{\text{media}}$  and  $\Delta P_{\text{throat}}$ .

### 4.3 Applying to the real filter design problem

The derived Eqs. (7)–(9) were applied to the actual filter design problem using a commercial filter of which  $VR$  and  $t$  are  $8.05 \times 10^{11} \text{ m}^2$  and  $0.38$  mm, respectively. With the  $U$  fixed at  $0.13$  m/s, Eq. (9) was used to obtain the optimum shape for  $h$  between  $3.2$  and  $6$  mm. The optimal shape for  $h = 3$  mm could not be obtained because the corresponding  $W_{\text{optim}}$  is less than  $1.08$  mm which is beyond the valid range listed in Table 2.

There are two things to be checked for the validation. First, it shall be verified whether Eqs. (7) and (8) are as accurate as the CFD simulations. Second, it should be checked whether the optimum geometry obtained by Eq. (9) really minimizes the pressure loss.

Figs. 7(a) and (b) show the results. The Fig. 7(a) shows the pressure drops of optimal filter shapes ( $W = W_{\text{optim}}$  and  $R = R_{\text{optim}}$ ) at the given filter heights. For example, when  $h$  is  $6$  mm, the CFD pressure drop of the corresponding optimum shape ( $W_{\text{optim}} = 1.2161$  mm and  $R_{\text{optim}} = 0.0626$  mm) is  $84.3$  Pa. The graph shows the accuracy of Eqs. (7) and (8) compared with CFD simulations. Both equations are accurate enough to replace CFD calculation, and Eq. (7) is better than Eq. (8). These conclusions are the same as those of the 8-fold cross-validation in Sec. 3.6. Fig. 7(b) compares the pressure loss calculated with CFD for three shapes: (1) optimal pitch, (2) increased pitch by  $10\%$ , (3) reduced pitch by  $-5\%$ . At the optimum pitch obtained by Eq. (9), the pressure loss is minimal; indicating that the optimum design equation is reliable.

## 5. Conclusions

This study delivered equations to estimate the pressure drop across the low-height, up to  $6$  mm, pleated filter and to identify the optimum filter design for given conditions. The procedures to obtain the equations are as follows. First, for accurate CFD calculations of filters, the suitable turbulent model was carefully selected using experimental and numerical data from references. Second, the two alternative pressure drop equations were derived using the regression analysis of the CFD results for arbitrary filter geometries and flowrates. The equations were determined to be accurate enough to replace CFD calculations. Third, the optimization algorithm was presented and applied to minimize filter pressure loss. Fourth, a set of optimum design equations was obtained through the optimization algorithm and regression analysis. Finally, all of the equations were applied to the actual filter design problem and verified using additional CFD simulation results.

Within the considered filter parameters' ranges, the order of importance of the parameters on pressure drop was analyzed:  $U > VR \gg h > W > t > R$ . Although  $R$  is the parameter with the least impact, it contributes to the change in pressure loss, thus it should be used as a design parameter for low-height pleated filters design. Furthermore, the novel contour plots were made to identify the optimum filter geometries instantaneously. The plots show how the filter geometry and flowrate affect the opti-

mal pitch that minimizes pressure drop. The optimum pitch increases with increasing flowrate and filter height and decreases with increasing filter medium resistance. Like the optimum pitch, the optimum folding radius is determined by the balance between the media resistance and the drag in pleat spacing.

Note that this study has limitations because it did not account for the effects of the filter surface roughness, the humidity, the permeability variation due to compression, and the dust. The limitations could be disregarded depending on the applications. For example, the effect of the dust could be neglected for the filters in CBRN mask canisters and cleanrooms since either the operation hour of the filter is very short or there is little dust in the air during the operation.

The results of this study provide useful information for designing pleated fibrous filters. With the derived pressure drop equations, engineers can predict pressure loss of the pleated filters without any CFD simulations. Using the optimization equation, they can optimize filter geometry immediately to minimize pressure drop. Since the derived equations are very accurate, this paper recommends using them even in multi-objective optimization.

## Acknowledgments

This work was supported by the Agency for Defense Development of Korea (UC190034GD).

## Nomenclature

### Abbreviation

AIC	: Akaike information criterion
CBRN	: Chemical biological radiological and nuclear
CFD	: Computational fluid dynamics
LHS	: Latin-hypercube sampling
MAE	: Mean absolute error
PAPR	: Powered air purifying respirator
RMSE	: Root mean square error (= root mean square deviation)
MAPE	: Mean absolute percentage error

### Symbols

$\theta$	: Filter folding angle [rad]
$\bar{\theta}$	: Dimensionless folding angle for LHS [-]
$\Delta P$	: Overall pressure drop across the filter [Pa]
$\Delta P_{\text{media}}$	: Pressure drop due to media resistance [Pa]
$\Delta P_{\text{throat}}$	: Pressure drop due to the drag in the pleat spacing [Pa]
$\mu$	: Air dynamic viscosity [ $\text{kg}\cdot\text{m}^{-1}\cdot\text{s}^{-1}$ ]
$\rho$	: Air density [ $\text{kg}\cdot\text{m}^{-3}$ ]
$h$	: Filter height [mm]
$L$	: Length of the filter centerline within half-pitch [mm]
$W$	: Filter pitch (= pleat width) [mm]
$W_{\text{optim}}$	: Optimum pitch minimizing pressure drop [mm]
$R$	: Filter folding radius [mm]

$R_{\text{optim}}$	: Optimum folding radius minimizing pressure drop [mm]
$Re_{\text{fiber}}$	: Fiber Reynolds number [-]
$r^2$	: Coefficient of determination [-]
$t$	: Filter media thickness [mm]
$U$	: Upstream velocity (= inlet velocity for CFD simulation) [ $\text{m}\cdot\text{s}^{-1}$ ]
$V_{\text{face}}$	: Filtration velocity (= face velocity) [ $\text{m}\cdot\text{s}^{-1}$ ]
$VR$	: Media resistance (= reciprocal of media permeability) [ $\text{m}^{-2}$ ]
$B$	: Breadth of narrow passage made by folding radius [mm]

## References

- [1] A. M. Saleh and H. V. Tafreshi, A simple semi-numerical model for designing pleated air filters under dust loading, *Sep. Purif. Technol.*, 137 (2014) 94-108.
- [2] F. Théron, A. Joubert and L. Le Coq, Numerical and experimental investigations of the influence of the pleat geometry on the pressure drop and velocity field of a pleated fibrous filter, *Sep. Purif. Technol.*, 182 (2017) 69-77.
- [3] M. I. Nazario, T. Mathanlal, M. P. Zorzano and J. Martin-Torres, Pressure optimized powered respirator (PROPER): a miniaturized wearable cleanroom and biosafety system for aerielly transmitted viral infections such as COVID-19, *HardwareX*, 8 (2020).
- [4] C. C. Li, Aerodynamic behavior of a gas mask canister containing two porous media, *Chem. Eng. Sci.*, 64 (8) (2009) 1832-1843.
- [5] S. G. A. Wood, N. Chakraborty, M. W. Smith and M. J. Summers, A computational fluid dynamics analysis of transient flow through a generic chemical biological radiological and nuclear respirator canister, *Chem. Eng. Res. Des.*, 142 (2019) 13-24.
- [6] Z. Feng, Z. Long and Q. Chen, Assessment of various CFD models for predicting airflow and pressure drop through pleated filter system, *Build. Environ.*, 75 (2014) 132-141.
- [7] D. R. Chen, D. Y. H. Pui and B. Y. H. Liu, Optimization of pleated filter designs using a finite-element numerical model, *Aerosol Sci. Technol.*, 23 (4) (1995) 579-590.
- [8] R. J. Wakeman, N. S. Hanspal, A. N. Waghode and V. Nas-sehi, Analysis of pleat crowding and medium compression in pleated cartridge filters, *Chem. Eng. Res. Des.*, 83 (10A) (2005) 1246-1255.
- [9] S. Li, S. Hu, B. Xie, H. Jin, J. Xin, F. Wang and F. Zhou, Influence of pleat geometry on the filtration and cleaning characteristics of filter media, *Sep. Purif. Technol.*, 210 (February 2018) (2019) 38-47.
- [10] M. Rebaï, M. Prat, M. Meireles, P. Schmitz and R. Baclet, A semi-analytical model for gas flow in pleated filters, *Chem. Eng. Sci.*, 65 (9) (2010) 2835-2846.
- [11] P. Tronville and R. Sala, Minimization of resistance in pleated-media air filter designs: empirical and CFD approaches, *HVAC R Res.*, 9 (1) (2003) 95-106.
- [12] S. Fotovati, S. A. Hosseini, H. V. Tafreshi and B. Pourdey-himi, Modeling instantaneous pressure drop of pleated thin filter media during dust loading, *Chem. Eng. Sci.*, 66 (18)

- (2011) 4036-4046.
- [13] S. Fotovati, H.V. Tafreshi and B. Pourdeyhimi, A macro-scale model for simulating pressure drop and collection efficiency of pleated filters over time, *Sep. Purif. Technol.*, 98 (2012) 344-355.
- [14] M. Rebai, M. Prat, M. Meireles, P. Schmitz and R. Baclet, Clogging modeling in pleated filters for gas filtration, *Chem. Eng. Res. Des.*, 88 (4) (2010) 476-486.
- [15] L. Oxarango, P. Schmitz and M. Quintard, Laminar flow in channels with wall suction or injection: a new model to study multi-channel filtration systems, *Chem. Eng. Sci.*, 59 (5) (2004) 1039-1051.
- [16] A. N. Waghode, N. S. Hanspal, R. J. Wakeman and V. Nassehi, Numerical analysis of medium compression and losses infiltration area in pleated membrane cartridge filters, *Chem. Eng. Commun.*, 194 (8) (2007) 1053-1064.
- [17] Y. H. Cheng and C. J. Tsai, Factors influencing pressure drop through a dust cake during filtration, *Aerosol Sci. Technol.*, 29 (4) (1998) 315-328.
- [18] T. Lücke and H. Fissan, The prediction of filtration performance of high efficiency gas filter elements, *Chem. Eng. Sci.*, 51 (8) (1996) 1199-1208.
- [19] A. Joubert, J. C. Laborde, L. Bouilloux, S. Callé-Chazelet and D. Thomas, Influence of humidity on clogging of flat and pleated HEPA filters, *Aerosol Sci. Technol.*, 44 (12) (2010) 1065-1076.
- [20] J. Li, S. Li and F. Zhou, Effect of moisture content in coal dust on filtration and cleaning performance of filters, *Physicochem. Probl. Miner. Process.*, 52 (1) (2016) 365-379.
- [21] J. H. Choi, S. J. Ha, Y. C. Bak and Y. O. Park, Particle size effect on the filtration drag of fly ash from a coal power plant, *Korean J. Chem. Eng.*, 19 (6) (2002) 1085-1090.
- [22] T. Frising, D. Thomas, D. Bémer and P. Contal, Clogging of fibrous filters by liquid aerosol particles: experimental and phenomenological modelling study, *Chem. Eng. Sci.*, 60 (10) (2005) 2751-2762.
- [23] M. D. McKay, R. J. Beckman and W. J. Conover, A comparison of three methods for selecting values of input variables in the analysis of output from a computer code, *Technometrics*, 21 (2) (1979) 239-245.
- [24] L. Del Fabbro, J. C. Laborde, P. Merlin and L. Ricciardi, Air flows and pressure drop modelling for different pleated industrial filters, *Filtr. Sep.*, 39 (1) (2002) 34-40.
- [25] N. J. Anderson, P. E. Cassidy, L. L. Janssen and D. R. Dengel, Peak inspiratory flows of adults exercising at light, moderate and heavy workloads, *J. Int. Soc. Respir. Prot.*, 23 (1943) (2006) 53-63.
- [26] J. Kiefer, Sequential minimax search for a maximum, *Proc. Am. Math. Soc.*, 4 (3) (1953) 502.
- [27] R. Storn and K. Price, Differential evolution—a simple and efficient heuristic for global optimization over continuous spaces, *J. Glob. Optim.*, 11 (4) (1997) 341-359.
- [28] Y. C. Su and C. C. Li, Computational fluid dynamics simulations and tests for improving industrial-grade gas mask canisters, *Adv. Mech. Eng.*, 7 (8) (2015) 1-14.
- [29] National Institute for Occupational Safety and Health (NIOSH), *Statement of Standard for Chemical, Biological, Radiological, and Nuclear (CBRN) Full Facepiece Air Purifying Respirator (APR)*, Washington, DC: NIOSH (2003).
- [30] I. P. S. Araújo, D. B. Costa and R. J. B. De Moraes, Identification and characterization of particulate matter concentrations at construction jobsites, *Sustainability* (2014) 7666-7688.

## Appendix

### A.1 Time scale of the dust caking and breakthrough of the CRBN canister

The service life of a gas mask is determined by the breakthrough time, not the pressure drop due to dust cake effect.

The reference time scale of the breakthrough time is shown by Su et al. [28]. They conducted HCN gas breakthrough test of a CBRN gas mask canister which conforms with the NIOSH 42 CFR Part 84 standard [29]. The breakthrough time of the gas mask was only 60.1 min at 30 L/min flowrate.

The reference time scale of the dust caking can be estimated through a calculation using experimental data from other literatures. This paper checked the time it takes for the pressure loss to increase by 10 % due to dust compared to a clean filter. For the calculation, the following values should be known: (1)  $\sigma_{\text{dust}} [\mu\text{g}/\text{m}^2]$  = the weight of dust per unit filtration area that increases the pressure loss by 10 %, (2)  $C_{\text{dust}} [\mu\text{g}/\text{m}^3]$  = the dust concentration in the battlefield where the CBRN gas mask is used, (3)  $Q$  = the breathing flow rate, and (4)  $A_{\text{filter}} [\text{m}^2]$  = the filter surface area.

1) Li et al. [9] measured the pressure loss due to the dust cake for 12 filters with different pleat shapes and materials. Using the experimental data, this paper checked the  $\sigma_{\text{dust}}$  was from  $1.78 \times 10^6 \mu\text{g}/\text{m}^2$  to  $9.13 \times 10^6 \mu\text{g}/\text{m}^2$ .

2) Since the concentration of dust on the battlefield is unknown, the dust concentration of the construction site was used instead. Araújo et al. [30] measured total suspended particulates (TSP) at three construction sites over nine days. The average was  $385.89 \mu\text{g}/\text{m}^3$  (=  $C_{\text{dust}}$ ).

3) This paper uses 30 L/min as the  $Q$  which was previously used in the breakthrough test by Su et al. [28].

4) The  $A_{\text{filter}}$  is  $4.925 \times 10^{-2} \text{m}^2$  when the radius of the filter layer is 51.5 mm [4],  $h = 6 \text{mm}$ ,  $p = 2 \text{mm}$ ,  $t = 0.38 \text{mm}$ , and  $R = 0.04 \text{mm}$ .

The time it takes for the pressure loss to increase by 10 % can be calculated as follows:

$$\text{Time} = \frac{\sigma_{\text{dust}} A_{\text{filter}}}{C_{\text{dust}} Q} \quad (\text{A.1})$$

The corresponding time is from 126.0 hr to 647.5 hr. Therefore, the dust caking time is much longer than the breakthrough time. Ergo, we can conclude that time is insufficient for the dust

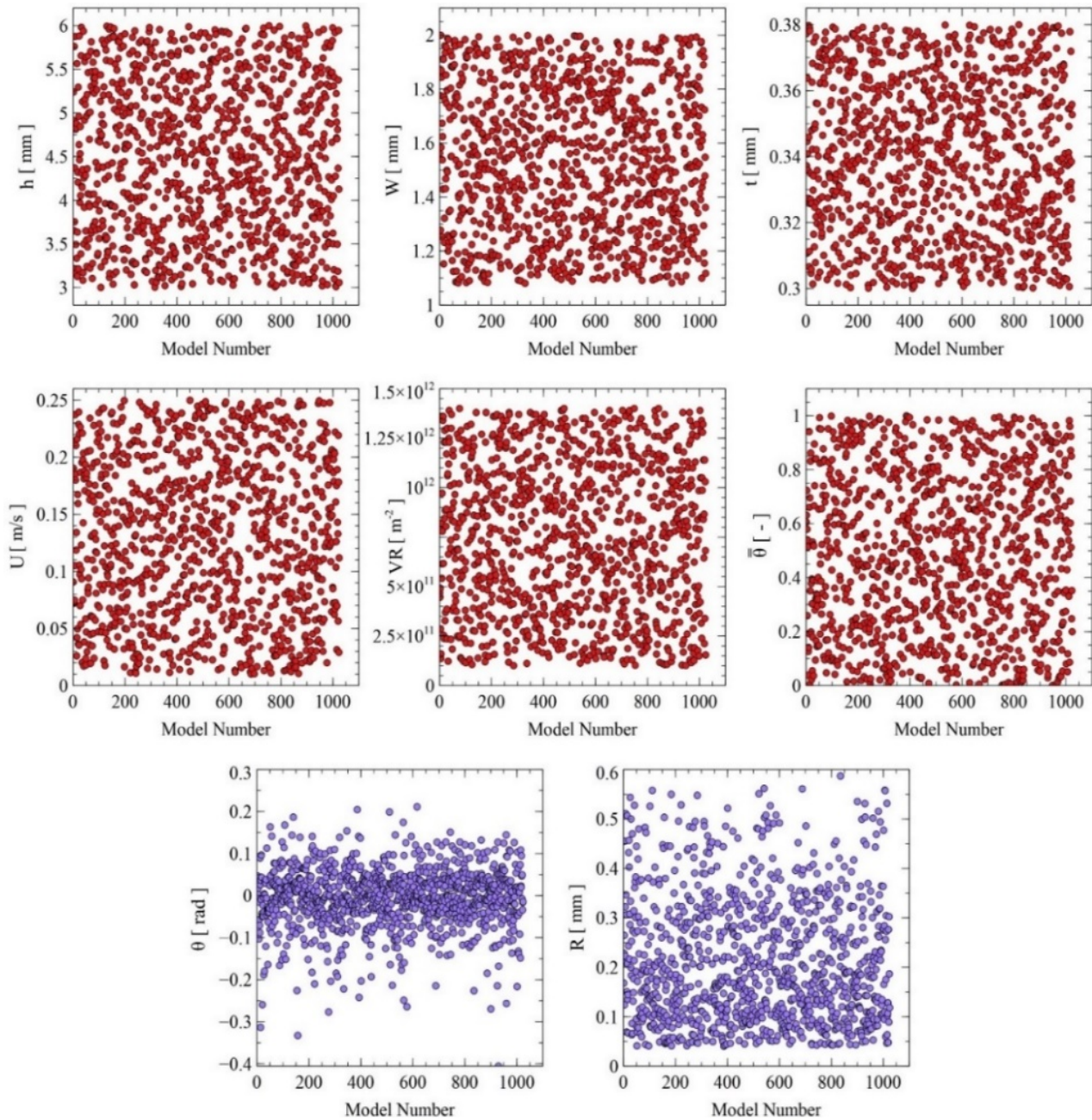


Fig. A.1. The results of Latin-hypercube sampling.

to stick to the filter surface within the service life of the CBRN gas mask.

## A.2 LHS sampling

Fig. A.1 shows the sampling results of the parameters for the considered range listed in Table 2. The red circles are the sampled design points extracted using the LHS method, while the blue circles represent the calculated design points using the red ones. As mentioned in Sec. 3.2, the ranges of R and  $\theta$  depend on other parameters, thus, it is impossible to extract R

and  $\theta$  directly. This paper first extracts the folding angle in dimensionless  $\bar{\theta}$  (red circle) as shown in Eq. (A.2):

$$\bar{\theta} = \frac{\theta_{\max} - \theta}{\theta_{\max} - \theta_{\min}} \quad (\text{A.2})$$

where  $\theta_{\max}$  and  $\theta_{\min}$  can be calculated using the method mentioned in Sec. 3.2. It is then converted into a dimensional  $\theta$  (blue circle). Finally, the folding radius R (blue circle) is calculated using Eq. (1).

### A.3 Mean factor levels and coefficients of equations

Table A.1. Mean factor levels and coefficients of the pressure drop equations, Eqs. (7) and (8).

Eq. (7)				Eq. (8)	
Factor ( $X_i$ or $X_i \cdot X_j$ )	Coefficient ( $C_i$ or $C_{ij}$ )	Factor ( $X_i$ or $X_i \cdot X_j$ )	Coefficient ( $C_i$ or $C_{ij}$ )	Factor ( $X_i$ or $X_i \cdot X_j$ )	Coefficient ( $C_i$ or $C_{ij}$ )
$\ln(U)$	1.317	$\ln(R)$	-1.936	$\ln(U)$	1.393
$\ln(VR)$	1.361	$\ln(R) \cdot \ln(B)$	$1.128 \times 10^{-1}$	$\ln(VR)$	$7.377 \times 10^{-1}$
$\ln(h)$	$-9.003 \times 10$	$\ln(h) \cdot \ln(R)$	3.474	$\ln(h)$	2.289
$\ln(W)$	-3.226	$\theta \cdot \ln(t)$	2.322	$\ln(W)$	-9.025
$\ln(t)$	5.184	$\ln(U) \cdot \ln(W)$	$-8.938 \times 10^{-2}$	$\ln(t)$	3.833
$\ln(VR) \cdot \ln(W)$	$2.233 \times 10^{-1}$	$\theta$	$4.704 \times 10$	$\ln(VR) \cdot \ln(W)$	$3.479 \times 10^{-1}$
$\ln(B)$	-4.300	$\ln(VR) \cdot \ln(U)$	$-8.915 \times 10^{-3}$	$\ln(VR) \cdot \ln(R)$	$-4.713 \times 10^{-2}$
$\ln(L)$	$9.352 \times 10$	$\ln(h) \cdot \ln(L)$	$1.241 \times 10^{-1}$	$\ln(h) \cdot \ln(R)$	$1.218 \times 10^{-1}$
$\ln(VR) \cdot \ln(B)$	$1.593 \times 10^{-1}$	$\ln(U) \cdot \ln(t)$	$6.858 \times 10^{-2}$	$\ln(VR) \cdot \ln(h)$	$-1.017 \times 10^{-1}$
$\ln(VR) \cdot \ln(R)$	$6.268 \times 10^{-2}$	$\ln(VR) \cdot \ln(t)$	$-1.626 \times 10^{-1}$	$\ln(h) \cdot \ln(W)$	$-4.791 \times 10^{-1}$
$\ln(VR) \cdot \ln(L)$	-3.687	$\ln(U) \cdot \ln(L)$	$6.504 \times 10^{-1}$	$\ln(W) \cdot \ln(t)$	$-6.853 \times 10^{-1}$
$\theta \cdot \ln(W)$	-5.149	$\theta \cdot \ln(U)$	$2.035 \times 10^{-1}$	$\ln(R)$	1.113
$\theta \cdot \ln(h)$	-6.458	$\ln(W) \cdot \ln(L)$	$-3.334 \times 10^{-1}$	$\ln(U) \cdot \ln(W)$	$-4.431 \times 10^{-2}$
$\ln(VR) \cdot \ln(h)$	3.511	$\theta \cdot \ln(L)$	7.310	$\ln(W) \cdot \ln(R)$	$-4.357 \times 10^{-2}$
$\ln(h) \cdot \ln(B)$	1.722	$\ln(U) \cdot \ln(h)$	$-6.314 \times 10^{-1}$	$\ln(VR) \cdot \ln(U)$	$-1.358 \times 10^{-2}$
$\ln(W) \cdot \ln(B)$	$3.709 \times 10^{-1}$	$\ln(R) \cdot \ln(L)$	-3.387	$\ln(VR) \cdot \ln(t)$	$-8.710 \times 10^{-2}$
$\theta \cdot \ln(VR)$	-1.591	(Intercept)	$-2.961 \times 10 = C_0$	(intercept)	$-1.139 \times 10 = C_0$
$\ln(L) \cdot \ln(B)$	-1.925				

Table A.2. Mean factor levels and coefficients of the optimization equation, Eq. (9).

$W_{\text{optim}}$ equation				$R_{\text{optim}}$ equation			
Factor ( $X_i$ or $X_i \cdot X_j$ )	Coefficient ( $C_i$ or $C_{ij}$ )	Factor ( $X_i$ or $X_i \cdot X_j$ )	Coefficient ( $C_i$ or $C_{ij}$ )	Factor ( $X_i$ or $X_i \cdot X_j$ )	Coefficient ( $C_i$ or $C_{ij}$ )	Factor ( $X_i$ or $X_i \cdot X_j$ )	Coefficient ( $C_i$ or $C_{ij}$ )
$\ln(VR)$	2.773	$t^2$	-2.986	$\ln(VR)$	$2.512 \times 10^{-1}$	$h^2 \cdot (\ln(VR))^2$	$5.318 \times 10^{-5}$
$h$	4.375	$t \cdot (\ln(VR))^2$	$-3.288 \times 10^{-2}$	$h$	$2.156 \times 10^{-1}$	$t^2$	$3.091 \times 10$
$t$	$-2.009 \times 10$	$h^2 \cdot \ln(U)$	$-7.973 \times 10^{-4}$	$h^2$	$1.528 \times 10^{-2}$	$(\ln(VR))^2 \cdot \ln(U)$	$-9.857 \times 10^{-5}$
$h \cdot \ln(VR)$	$-2.704 \times 10^{-1}$	$(\ln(U))^2$	$-1.042 \times 10^{-3}$	$h \cdot \ln(VR)$	$-3.214 \times 10^{-3}$	$\ln(VR) \cdot \ln(U)$	$5.097 \times 10^{-3}$
$h^2$	$-8.836 \times 10^{-2}$	$(\ln(VR))^2 \cdot \ln(U)$	$-6.107 \times 10^{-4}$	$t$	$-2.215 \times 10$	$t^2 \cdot (\ln(VR))^2$	$4.710 \times 10^{-2}$
$(\ln(VR))^2$	$-9.994 \times 10^{-2}$	$t^2 \cdot \ln(U)$	$2.981 \times 10^{-1}$	$t \cdot h$	$-2.546 \times 10^{-1}$	$(\ln(VR))^3$	$2.710 \times 10^{-4}$
$\ln(U)$	$-3.413 \times 10^{-1}$	$t^2 \cdot (\ln(VR))^2$	$1.163 \times 10^{-3}$	$\ln(U)$	$-6.404 \times 10^{-2}$	$t^2 \cdot \ln(VR)$	-2.478
$t \cdot \ln(VR)$	1.702	$t^3$	1.501	$(\ln(VR))^2$	$-1.536 \times 10^{-2}$	$(\ln(U))^2$	$-1.553 \times 10^{-4}$
$h \cdot \ln(U)$	$1.169 \times 10^{-2}$	$t^2 \cdot h$	$2.952 \times 10^{-1}$	$t \cdot \ln(VR)$	1.748	$t^2 \cdot h$	$5.527 \times 10^{-1}$
$t \cdot h$	$1.317 \times 10^{-1}$	$(\ln(VR))^3$	$1.218 \times 10^{-3}$	$h \cdot \ln(U)$	$1.697 \times 10^{-3}$	$t^2 \cdot \ln(U)$	$2.975 \times 10^{-2}$
$h^2 \cdot \ln(VR)$	$2.395 \times 10^{-3}$	$h^2 \cdot (\ln(U))^2$	$-4.046 \times 10^{-5}$	$h^3$	$5.151 \times 10^{-4}$	$t^2 \cdot h^2$	$-5.199 \times 10^{-2}$
$h \cdot (\ln(VR))^2$	$4.208 \times 10^{-3}$	$(\ln(VR))^2 \cdot (\ln(U))^2$	$7.523 \times 10^{-7}$	$t \cdot \ln(U)$	$-2.801 \times 10^{-2}$	$h^2 \cdot (\ln(U))^2$	$-1.886 \times 10^{-6}$
$t \cdot \ln(U)$	$-2.327 \times 10^{-1}$	$h \cdot (\ln(U))^2$	$3.527 \times 10^{-4}$	$t \cdot h^2$	$2.549 \times 10^{-2}$	$t \cdot (\ln(VR))^2$	$-3.331 \times 10^{-2}$
$h^3$	$1.423 \times 10^{-3}$	(intercept)	$-2.585 \times 10 = C_0$	$h^2 \cdot \ln(VR)$	$-2.446 \times 10^{-3}$	$(\ln(VR))^2 \cdot (\ln(U))^2$	$2.465 \times 10^{-7}$
$\ln(VR) \cdot \ln(U)$	$2.985 \times 10^{-2}$			$h \cdot (\ln(VR))^2$	$-6.850 \times 10^{-5}$	(intercept)	$-1.024 = C_0$
$t^2 \cdot h^2$	$-3.515 \times 10^{-2}$			$h^2 \cdot \ln(U)$	$-1.357 \times 10^{-4}$		



**Paul Choi** received his Bachelor's degree in Mechanical Engineering from Kyung Hee University in 2021. He is currently a battery engineer at LG Energy Solution, Ltd. His research is the optimization of the electrode slurry coating process using CFD and programming.



**Christian Ariane Santos** is a researcher at the Fine Particle Flow Laboratory in Kyung Hee University, Yongin, South Korea. She has a master's degree in Environmental Engineering.



**Min-Kun Kim** is a Senior Researcher in the Agency for Defense Development, Daejeon, South Korea. He earned his Ph.D. degree in School of Chemical and Biological Engineering from Seoul National University. His current research field is CBRN protection/decontamination engineering.



**Do-Young Hong** is a Principal Researcher at the Korea Research Institute of Chemical Technology (KRICT). He joined the faculty there in 2013. He received his Ph.D. (2006) in chemical engineering from Hanyang University. He then conducted postdoctoral studies in the lab of Prof. C.W. Jones at the Georgia Institute of Technology (2007) and the lab of Prof. A. Bhan at the University of Minnesota (2010). His present research areas are in catalysis for biomass and waste plastics and gas sorption based on organic-inorganic hybrid materials.



**Hyunsook Jung** is a Principal Researcher in the Chem-Bio Technology Center, Agency for Defense Development, Daejeon, South Korea. She earned her Ph.D. degree in Chemistry from Texas A&M University at College Station.



**Junemo Koo** is a Professor in the Department of Mechanical Engineering, Kyung Hee University, Yongin, South Korea. He earned his Ph.D. degree in Mechanical and Aerospace Engineering from North Carolina State University.